

# Reciprocity-gap misfit functional for Distributed Acoustic Sensing, combining data from passive and active sources

Florian Faucher\*      Maarten V. de Hoop†      Otmar Scherzer‡

## Abstract

Quantitative imaging of sub-surface Earth’s properties in elastic media is performed from Distributed Acoustic Sensing data. A new misfit functional based upon the *reciprocity-gap* is designed, taking cross-correlations of displacement and strain, and these products further associate an observation with a simulation. In comparison with other misfit functionals, this one has the advantage to only require little a-priori information on the exciting sources. In particular, the misfit criterion enables the use of data from regional earthquakes (teleseismic events can be included as well), followed by exploration data to perform a multi-resolution reconstruction. The data from regional earthquakes contain the low-frequency content which is missing in the exploration ones, allowing for the recovery of the long spatial wavelength, even with very few sources. These data are used to build prior models for the subsequent reconstruction from the higher-frequency exploration data. This gives the elastic Full Reciprocity-gap Waveform Inversion method, and we demonstrate its performance with a pilot experiment for elastic isotropic reconstruction.

## 1 Introduction

Adjoint tomography and full waveform inversion in global and exploration seismology have, over the past two decades, dramatically improved our capabilities to estimate material properties and structure of Earth’s interior, e.g., Tarantola (1984); Gauthier et al. (1986); Pratt et al. (1998); Ravaut et al. (2004); Tromp et al. (2005); Fichtner et al. (2006a,b); Tape et al. (2007); Liu and Tromp (2008); Fichtner et al. (2008); Luo et al. (2009); Virieux and Operto (2009); Brossier et al. (2009); Fichtner (2010); Komatitsch et al. (2016) and Modrak and Tromp (2016). In exploration seismology, the absence of relatively low frequencies in the data limits basic resolution (Gauthier et al., 1986; Mora, 1987; Luo and Schuster, 1991; Fichtner et al., 2008; Ten Kroode et al., 2013) unless some prior information is employed (Bunks et al., 1995). With the introduction of Distributed Acoustic Sensing (DAS) (Mestayer et al., 2011; Cox et al., 2012; Daley et al., 2013; Ajo-Franklin et al., 2015), a new opportunity has been provided to use (passive-source) global and (active-source) exploration seismic data in an integrated manner, on a regional scale, overcoming, in principle, the resolution limitations. This is the subject of this paper.

In adjoint tomography and full waveform inversion, here collectively referred to as FWI, the identification of Earth’s parameters can be conducted via a minimization problem, where

---

\*Faculty of Mathematics, University of Vienna, Oskar-Morgenstern-Platz 1, A-1090 Vienna, Austria (florian.faucher@univie.ac.at).

†Department of Computational and Applied Mathematics and Department of Earth Science, Rice University, Houston TX 77005, USA.

‡Johann Radon Institute for Computational and Applied Mathematics (RICAM), Altenbergerstraße 69 A-4040, Linz, Austria.

one optimizes a misfit criterion between observed data and simulations. It was first developed for the wave equation by [Bamberger et al. \(1977, 1979\)](#); [Lailly \(1983\)](#) and [Tarantola \(1984\)](#), while the time-harmonic formulation was proposed by [Pratt et al. \(1996; 1998; 1999\)](#). The main difficulty comes from the local minima in the misfit functional, which are due to the inaccurate background velocity information that causes phase shifts between observed and computed signals. This issue of cycle-skipping has motivated several studies aiming at mitigating their occurrences, e.g., [Gauthier et al. \(1986\)](#); [Luo and Schuster \(1991\)](#); [Bunks et al. \(1995\)](#); [Clément et al. \(2001\)](#); [Fichtner et al. \(2008\)](#); [Virieux and Operto \(2009\)](#) and [Faucher et al. \(2020b\)](#). In particular, the frequency progression and multi-resolution strategy ([Bunks et al., 1995](#); [Sirgue and Pratt, 2004](#)) have been widely applied. The use of different parametrizations of the inverse problem has also been proposed by, e.g., [Symes and Carazzone \(1991\)](#) and [Clément et al. \(2001\)](#), at the cost of an increased computational complexity ([Faucher et al., 2020b](#)). The presence of local minima in the misfit function and the convergence of iterative methods have also been studied theoretically through conditional, stability estimates ([Beretta et al., 2014, 2017](#)) in a multi-resolution framework ([de Hoop et al., 2015](#); [Beretta et al., 2016](#)). However, if “true” Earth models are restricted to be piecewise smooth, there is a precise way to recover these through scattering control, thus avoiding optimization ([Caday et al., 2019](#)).

While the misfit functional traditionally relies on the difference between the full observations and the simulations, several alternatives have been investigated. These include criteria based on the phase and envelope of the signal ([Fichtner et al., 2008](#)), the cross-correlation of signals ([Luo and Schuster, 1991](#); [Van Leeuwen and Mulder, 2010](#)), the  $L1$  ([Brossier et al., 2010](#)) and the optimal transport distance by ([Métivier et al., 2016](#); [Yang et al., 2018](#)). In this paper, we propose a new functional based on the reciprocity theorem of time-correlation type ([de Hoop and de Hoop, 2000](#)), using the displacement and the normal stress. Then, our misfit is equivalently written in terms of the strain, replacing the normal stress. We coin it the *reciprocity-gap* functional, following works on acoustic inverse scattering by [Kohn and Vogelius \(1985\)](#) and [Colton and Haddar \(2005\)](#). [Alessandrini et al. \(2019\)](#) and [Faucher et al. \(2020a\)](#) establish theoretical results for guaranteed recovery and provide applications in acoustic marine seismic. Time correlation- and convolution-based functionals have also been studied by, e.g., [Van Leeuwen and Mulder \(2010\)](#); [Choi and Alkhalifah \(2011\)](#) and [Montagner et al. \(2012\)](#). In addition to correlate the displacement and the stress, our misfit function also combines observation and simulation data.

The key feature of our underlying Full Reciprocity-gap Waveform Inversion (FRgWI) method is that the misfit functional we introduce does not require knowledge (location and characteristics) of the passive and active sources (that is, the sources from which the measurements are extracted). We exploit these properties in integrating regional earthquakes and exploration data from a natural multi-resolution perspective, that we illustrate in [Figure 1](#). Regional earthquakes (and teleseismic) data contain the very low frequencies that are missing, and needed, in the exploration setting. Furthermore, we shall see that a small number of sources is sufficient to extract the long wavelength profile of the media. In seismic inversion using data from teleseismic events (distant earthquakes), it is assumed that the (teleseismic) source is sufficiently distant from the area of interest so that the incoming waves that illuminate this area can be considered as plane waves, cf. [Bostock et al. \(2001\)](#) and [Tromp \(2019\)](#). Under such an assumption, the characterization of the distant source is not needed for imaging and, for instance, reconstructions using teleseismic data is carried out by [Shragge et al. \(2001\)](#) and [Rondenay et al. \(2001\)](#) assuming the Born approximation, and by [Beller et al. \(2018b,a\)](#) using a least-squares misfit function. The FRgWI method is more general as no assumption is needed to characterize the passive source: The method supports all types

of passive sources (distant or near from the area of interest, i.e., plane wave or point-source illumination), without requiring a priori specification; we illustrate in the experiment with local earthquake data (see Figure 1a).

The benefits of the elastic reciprocity-gap waveform inversion comes at the price of taking measurements of both the displacement *and* of certain components of the strain tensor. While measurements of the displacement are common with (string) geophones (which can be buried, cf. Drijkoningen et al. (2006)), the possibility to measure the strain can be envisioned with DAS (Daley et al., 2013; Ajo-Franklin et al., 2015; Lindsey et al., 2020). Depending on the configuration of the cable, different components of the strain can be retrieved, as highlighted by Lim Chen Ning and Sava (2018); see, in particular, their Figure 2. Helical and straight cables provide the necessary features to extract the strain components (Innanen, 2017; Lim Chen Ning and Sava, 2018). Comparisons between geophones and DAS data have been carried out by Mateeva et al. (2013) and Spikes et al. (2019); here, we use both data jointly. Earthquakes (in particular teleseismic events) have been recorded using DAS system by Lindsey et al. (2017); Jousset et al. (2018) and Ajo-Franklin et al. (2019), hence including long-period signals with low-frequency contents, see Lindsey et al. (2020). The comparison between earthquake data recorded by DAS and geophones is further studied by Wang et al. (2018) while Lellouch et al. (2019) use DAS data from earthquake to estimate velocity profiles. While the recording and use of such data still remain in its early stages, our work proposes a conceptual study that introduces a new method to fully exploit them.

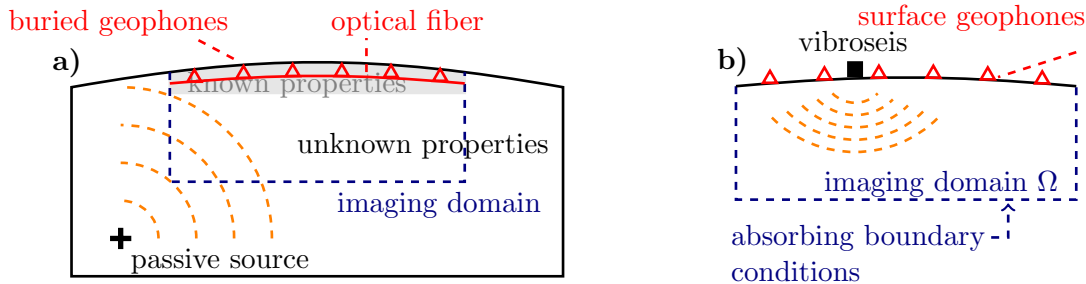


Figure 1: Illustration of the configuration where (a) the source of the regional earthquake is allowed to lie outside of the (b) computational domain in exploration. In order to avoid the free-surface condition where the normal stress is zero, the devices are considered slightly buried, and we assume the knowledge of the physical properties in the near surface area (in grey) for FRgWI.

The novelties of our work are (1) the introduction of the reciprocity-gap misfit functional for elastic wave propagation which allows, from the DAS acquisition system, the (2) multi-resolution reconstruction using observed data from (2a) events from passive sources (low-frequency), and (2b) exploration acquisition (high-frequency). We first detail the method, which fundamental feature is to require only little a-priori knowledge regarding the sources. Then we demonstrate the performance of an approach based on our functional with a computational experiment. Here, the data from regional events are first used to recover the coarse-scale background model. Next, the exploration data are used to retrieve the finer scales. While we need the knowledge of the elastic parameters at and very near the surface (where the optical fibers are buried), existing exploration data can be used to recover these, thus further strengthening the interplay between regional earthquakes and exploration data.

## 2 Methodology

We consider the non-linear seismic imaging problem from measurements of waves and rely on an iterative minimization algorithm for the recovery of sub-surface elastic properties. We introduce a misfit functional based on the *reciprocity-gap* formula, which uses combinations of measurements and simulations. It uses measurements of the strain, and enables the use of data from arbitrary probing sources. Note that while we formulate the method in the frequency domain, it can be similarly applied in the time domain.

### 2.1 Modeling the Data

We consider the propagation of time-harmonic waves in an elastic medium, given in terms of the vectorial displacement field  $\mathbf{u}$  and of the stress tensor of order two  $\underline{\sigma}$  such that, at frequency  $\omega$  and for an (internal) source  $\mathbf{f}$ , we have

$$\nabla \cdot \underline{\sigma}(\mathbf{x}, \omega) + \omega^2 \rho(\mathbf{x}) \mathbf{u}(\mathbf{x}, \omega) = \mathbf{f}(\mathbf{x}), \quad \text{in the domain } \Omega. \quad (1)$$

Here,  $\rho$  is the material density and  $\mathbf{x}$  represents the space coordinates. In linear elasticity, the stress tensor is related to the strain tensor  $\underline{\epsilon}$  by Hooke's law:

$$\underline{\sigma}(\mathbf{x}, \omega) = \underline{\underline{C}}(\mathbf{x}, \omega) \underline{\epsilon}(\mathbf{x}, \omega), \quad \text{with } \underline{\epsilon} = \frac{1}{2} \left( \nabla \mathbf{u} + (\nabla \mathbf{u})^T \right), \quad (2)$$

where  $^T$  indicates the transpose of a matrix. The physical properties of the medium are encoded in the elasticity tensor of order four  $\underline{\underline{C}}$  which, in the case of isotropy, reduces to the Lamé parameters  $\lambda$  and  $\mu$ , such that equation 2 writes as,

$$\underline{\sigma} = \lambda \text{Tr}(\underline{\epsilon}) I_d + 2 \mu \underline{\epsilon}, \quad (3)$$

where  $\text{Tr}$  denotes the trace, and  $I_d$  the identity matrix. We further recall the P- and S-wave speeds, respectively  $c_p$  and  $c_s$ , as a function of the Lamé parameters:

$$c_p = \sqrt{(\lambda + 2\mu)/\rho}, \quad c_s = \sqrt{\mu/\rho}. \quad (4)$$

At the boundary of the domain  $\Omega$ , we consider a free surface between the air and the ground where, in the absence of a source,  $\underline{\sigma} \cdot \mathbf{n} = 0$ . We impose absorbing boundary conditions at the other boundaries (see Figure 1b), we refer to, e.g., [Givoli and Keller \(1990\)](#) and [Higdon \(1991\)](#).

The forward problem  $\mathcal{F}$  is defined as a mapping from the model to the data, that is, it gives the solution to the wave equation at the location of the receivers for a given physical model  $\mathbf{m}$  (for instance,  $\mathbf{m} = (\lambda, \mu, \rho)$  for elastic isotropy). We write the forward problem in terms of the displacement and of the normal stress (traction) and denote by  $X_{\text{rcv}}$  the receiver line. Considering  $\mathbf{f}_k$  the source used for the simulations, we define at frequency  $\omega$ ,

$$\begin{aligned} \mathcal{F}(\mathbf{f}_k, \mathbf{m}, \omega) &= \left\{ \mathcal{F}_{\mathbf{u}}(\mathbf{f}_k, \mathbf{m}, \omega); \mathcal{F}_{\underline{\sigma} \cdot \mathbf{n}}(\mathbf{f}_k, \mathbf{m}, \omega) \right\} \\ &= \left\{ \mathbf{u}(\mathbf{x}, \mathbf{f}_k, \mathbf{m}, \omega); \underline{\sigma}(\mathbf{x}, \mathbf{f}_k, \mathbf{m}, \omega) \cdot \mathbf{n}; \mathbf{x} \in X_{\text{rcv}} \right\}. \end{aligned} \quad (5)$$

The index notations  $\mathcal{F}_{\mathbf{u}}$  and  $\mathcal{F}_{\underline{\sigma} \cdot \mathbf{n}}$  refer to the displacement or the normal stress data respectively, and  $\mathbf{n}$  is the *principal* normal vector. The normal stress further relates to the observables in DAS acquisition (the strain) via the Hooke's law in equation 2 (see the dedicated section below).

## 2.2 Full Reciprocity-gap Waveform Inversion (FRgWI): Misfit Functional

The quantitative reconstruction of the subsurface elastic properties is recast as an iterative minimization problem following the FWI approach and we design a specific misfit functional based upon the *reciprocity gap*. We first write the functional in terms of the stress tensor, and equivalently use the strain data to relate to the DAS acquisition system in the next section.

We denote by  $\mathbf{d}_u(\mathbf{g})$  and  $\mathbf{d}_{\sigma \cdot \mathbf{n}}(\mathbf{g})$  the measurements associated to a source  $\mathbf{g}$ , for the displacement and the normal stress respectively. That is,  $\mathbf{g}$  and  $\mathbf{f}$  (from equation 5) stand for the sources (right-hand sides of equation 1) that generate the observations and the simulations, respectively. It means that  $\mathbf{g}$  represents the “real” or “observational” sources of the measured events (e.g., a passive source), which can be unknown. On the other hand,  $\mathbf{f}$  in equation 5 stands for the “artificial” or “computational” sources, used for the simulations, and their positions are chosen independently. It means that both set of sources ( $\mathbf{g}$  and  $\mathbf{f}$ ) can, but *do not have to* be the same.

Omitting the space dependency for clarity, the reciprocity-gap misfit functional in terms of the stress is defined such that,

$$\mathcal{J}_\sigma(\mathbf{m}, \omega) = \frac{1}{2} \sum_{j=1}^{n_{\text{src}}^{\text{sim}}} \sum_{k=1}^{n_{\text{src}}^{\text{obs}}} \left\| \int_{X_{\text{rcv}}} (\mathbf{u}(\mathbf{f}_j, \mathbf{m}, \omega) \cdot \mathbf{d}_{\sigma \cdot \mathbf{n}}(\mathbf{g}_k, \omega) - \mathbf{d}_u(\mathbf{g}_k, \omega) \cdot (\underline{\sigma}(\mathbf{f}_j, \mathbf{m}, \omega) \cdot \mathbf{n})) dx \right\|^2, \quad (6)$$

where  $\|\cdot\|^2$  is the complex  $L^2$  inner product. Because of the correlation of an observation  $\mathbf{d}$  and a simulation  $(\mathbf{u}, \underline{\sigma})$  in the misfit, the real sources  $\mathbf{g}$  are not explicitly needed to construct the functional. It allows for the independent selection of the computational sources  $\mathbf{f}$ , and for a different number of observational sources,  $n_{\text{src}}^{\text{obs}}$ , compared to the number of computational ones,  $n_{\text{src}}^{\text{sim}}$ . Then, the two sums in equation 6 imply that each of the real source is tested against all of the computational ones. For the discretization of the integral along the line of receivers, we can use a sum over discrete receiver locations or, for different configurations, a weighted sum (e.g., quadrature rule), see [Montagner et al. \(2012\)](#). The misfit functional is derived from the Green’s identity, which allows to replace the surface integral (along the line of receivers) by a volume one (introducing the divergence of the stress). Then, using the state equations 1 and 2, the functional relates to the comparison of the physical properties in the interior; we refer to the derivation given in the Appendix A of [Faucher et al. \(2020a\)](#) for more details.

The essence of this approach is two fold: first, it does not compare the observations and simulations directly but instead works with their cross-correlations (which, in the frequency domain, amounts to a multiplication). Secondly, each product is made of different fields (i.e., displacement and strain). Consequently, the set of sources for the data ( $\mathbf{g}_k$ ) and for the simulations ( $\mathbf{f}_j$ ) is separated. The positions of the sources that generate the measurements are not needed to define the misfit and the simulations can use arbitrary sources (in terms of their positions and functions).

## 2.3 From DAS acquisition to Reciprocity-gap Inversion

Our misfit functional in equation 6 is defined in terms of the displacement and of the normal stress. However, the strain can be retrieved from DAS acquisition system ([Lim Chen Ning and Sava, 2018](#)). Therefore, we have to rewrite equation 6 in terms of the strain. It suffices to replace the stress in equation 6 using Hooke’s law equation 2. Nonetheless, it means that the medium parameters (contained in  $\underline{\underline{C}}$ ) must be known at the location of the receivers, and that all the strain components must be measured.

In the case of elastic isotropy where the Hooke's law equation 3 prevails, the component of the normal stress in the direction  $\mathbf{d} = \{x, y, z\}$  is given by,

$$[\underline{\sigma} \cdot \mathbf{n}]_{\mathbf{d}} = 2\mu \sum_j \epsilon_{dj} \mathbf{n}_j + \lambda \text{Tr}(\underline{\epsilon}) \mathbf{n}_{\mathbf{d}} = 2\mu [\underline{\epsilon} \cdot \mathbf{n}]_{\mathbf{d}} + \lambda \left( \sum_j \epsilon_{jj} \right) \mathbf{n}_{\mathbf{d}}. \quad (7)$$

To write the reciprocity-gap formula with the normal stress components we require, in terms of the strain (i.e., the observables in DAS acquisition),

1. measurements of the normal strain  $\underline{\epsilon} \cdot \mathbf{n}$ ,
2. measurements of the trace of the strain tensor (or the diagonal coefficients  $\epsilon_{jj}$ ),
3. the values of  $\lambda_0(\mathbf{x})$  and  $\mu_0(\mathbf{x})$  at the position of the receivers  $\mathbf{x} \in X_{\text{rcv}}$ .

Replacing the normal stress in equation 6 with the strain using equation 7, we can equivalently use the misfit functional in terms of the strain, which amounts, under isotropy, to

$$\mathcal{J}(\mathbf{m}) = \frac{1}{2} \sum_{j=1}^{n_{\text{src}}^{\text{sim}}} \sum_{k=1}^{n_{\text{src}}^{\text{obs}}} \left\| \int_{X_{\text{rcv}}} \left( \mathbf{u}(\mathbf{f}_j, \mathbf{m}) \cdot \left( 2\mu_0 \mathbf{d}_{\epsilon}(\mathbf{g}_k) \cdot \mathbf{n} + \lambda_0 \text{Tr}(\mathbf{d}_{\epsilon}(\mathbf{g}_k)) \mathbf{n} \right) - \mathbf{d}_{\mathbf{u}}(\mathbf{g}_k) \cdot \left( 2\mu_0 \underline{\epsilon}(\mathbf{f}_j, \mathbf{m}) \cdot \mathbf{n} + \lambda_0 \text{Tr}(\underline{\epsilon}(\mathbf{f}_j, \mathbf{m})) \mathbf{n} \right) \right) \mathbf{d} \mathbf{x} \right\|^2, \quad (8)$$

where  $\lambda_0$  and  $\mu_0$  are the known Lamé parameters at the position of the receivers, and  $\mathbf{d}_{\epsilon}(\mathbf{g})$  refers to the measurements of the strain associated to a source  $\mathbf{g}$ .

## 2.4 Combined Data Inversion

Data obtained for seismic exploration can be generated by vibroseis trucks, explosions or air guns. It usually consists in several hundreds or thousands of independent point-sources at the surface, giving reflection data in general. In the case of regional earthquakes or teleseismic events, the source can be several to hundreds of kilometers below the Earth's surface and such events are not controlled. In addition, while the source of an earthquake is characterized by the moment tensor, the vibroseis truck imposes a Neumann boundary condition (via the traction), see, e.g., [Baeten \(1989\)](#); [Aki and Richards \(2002\)](#); [Carcione \(2007\)](#) and [Shi et al. \(2019\)](#). Let us first note that the FRgWI method does not require the characterization of the observational (real) sources and one can use a dense set of computational sources to compensate for a sparse observational set, as highlighted by [Faucher et al. \(2020a\)](#).

In exploration seismic, the peak frequency of the source lays, at least, in the 15–20 Hz range, resulting in unusable (noisy) low-frequency content. On the contrary, the data from earthquakes contain signal of very low frequencies (even below 1 mHz). Therefore, the iterative minimization is conducted following these two steps:

1. we minimize  $\mathcal{J}$  using data from regional events for  $\mathbf{d}_{\mathbf{u}}$  and  $\mathbf{d}_{\epsilon}$ . This corresponds to a few sources relatively far from the domain of interest, but where the low-frequency content is usable.
2. From the low-frequency model built after step 1, we minimize  $\mathcal{J}$  using the exploration data for  $\mathbf{d}_{\mathbf{u}}$  and  $\mathbf{d}_{\epsilon}$ . Here, the acquisition is denser and the frequency content higher, to recover the finer details of the models.



It is crucial that, numerically speaking, steps 1 and 2 do not require a different computational domain. FRgWI works with arbitrary observational sources and, here, they are taken outside of the computational area. That is, the computational domain only consists of the exploration part, as illustrated in Figure 1. As an alternative, one can perform local updates after a computation on the global domain, e.g., Robertsson and Chapman (2000) and Masson and Romanowicz (2017).

## 2.5 Gradient Computation

The computation of the gradient of the misfit functional with respect to the parameters is based on the adjoint-state method, derived in the work of Lions (1971) and Glowinski (1985), and implemented by Chavent (1974); it is reviewed in the context of geophysics by Plessix (2006). In the adjoint-state method, the gradient of the misfit is computed from the adjoint of the forward problem with specific right-hand sides: the *backward* problem. These new right-hand sides are further referred to as the ‘*adjoint sources*’. The method is also at the heart of the adjoint-tomography technique in seismology (Tromp et al., 2005; Fichtner et al., 2006a,b; Tape et al., 2007; Bozdağ et al., 2016). It can also be used for the computations of second-order derivatives, see, e.g., Wang et al. (1992); Fichtner and Trampert (2011) and Métivier et al. (2013).

For the sake of conciseness, we shall only detail the adjoint-sources, which are specific to the misfit functional, and refer the readers to, e.g., Pratt et al. (1998); Plessix (2006); Chavent (2010); Alessandrini et al. (2019) and Barucq et al. (2019) for details of the method in seismic applications. The adjoint-sources are given by the derivatives of the misfit functional with respect to each component of the wavefield (here,  $\mathbf{u}$  and  $\underline{\sigma}$ ). For each of the *computational* sources  $\mathbf{f}_j$  in equation 6 corresponds a backward problem where each of the unknowns has a right-hand side  $W_\bullet$ , where  $\bullet$  refers to the component. Using  $\mathbf{d} = \{x, y, z\}$  to denote the direction (e.g.,  $W_{u_x}$  is associated with  $u_x$ ), the right-hand sides are given by, for  $\mathbf{x} \in X_{\text{rcv}}$ ,

$$\left\{ \begin{array}{l} W_{u_{\mathbf{d}}}(\mathbf{f}_j, \mathbf{x}) := \sum_{k=1}^{n_{\text{src}}^{\text{obs}}} \bar{\eta}(\mathbf{f}_j, \mathbf{g}_k) (\mathbf{d}_\sigma(\mathbf{g}_k, \mathbf{x}))_{\mathbf{d}} , \\ W_{\underline{\sigma}_{\mathbf{d}\mathbf{d}}}(\mathbf{f}_j, \mathbf{x}) := - \sum_{k=1}^{n_{\text{src}}^{\text{obs}}} \bar{\eta}(\mathbf{f}_j, \mathbf{g}_k) (\mathbf{d}_u(\mathbf{g}_k, \mathbf{x}))_{\mathbf{d}} \mathbf{n}_{\mathbf{d}} , \\ W_{\underline{\sigma}_{\mathbf{d}_1\mathbf{d}_2}}(\mathbf{f}_j, \mathbf{x}) := - \sum_{k=1}^{n_{\text{src}}^{\text{obs}}} \bar{\eta}(\mathbf{f}_j, \mathbf{g}_k) \sum_{\mathbf{d}_1 \neq \mathbf{d}_2} (\mathbf{d}_u(\mathbf{g}_k, \mathbf{x}))_{\mathbf{d}_1} \mathbf{n}_{\mathbf{d}_2} , \quad \text{for } \mathbf{d}_1 \neq \mathbf{d}_2 , \end{array} \right. \quad (9)$$

with

$$\eta(\mathbf{f}_j, \mathbf{g}_k) = \int_{X_{\text{rcv}}} \left( \mathbf{u}(\mathbf{f}_j, \mathbf{x}, \mathbf{m}) \cdot \mathbf{d}_\sigma(\mathbf{g}_k, \mathbf{x}) - \mathbf{d}_u(\mathbf{g}_k, \mathbf{x}) \cdot (\underline{\sigma}(\mathbf{x}, \mathbf{f}_j, \mathbf{m}) \cdot \mathbf{n}) \right) d\mathbf{x} , \quad (10)$$

using  $\bar{\cdot}$  to denote the complex conjugation. We see that each of the adjoint-sources take the contribution from *all* the measurement sources ( $\mathbf{g}_k$ ) that is, from all the observed data. Eventually, the gradient is obtained combining the forward and backward solutions (Pratt et al., 1998).

The reciprocity-gap misfit functional can also be written from data at the surface, for instance in the exploration settings where the source is the traction,  $\underline{\sigma} \cdot \mathbf{n}$ , imposed by the vibroseis (Baeten, 1989). In this case, with displacement data acquired by surface geophones, it gives the Neumann-to-Dirichlet map (Shi et al., 2019), which graph forms the necessary

Cauchy data for reciprocity gap (i.e., displacement and normal stress). Then, the misfit functional in equation 6 is written by replacing the values of the normal stress by the imposed source traction, such that,

$$\mathcal{J}_{\text{surface}}(\mathbf{m}) = \frac{1}{2} \sum_{j=1}^{n_{\text{src}}^{\text{sim}}} \sum_{k=1}^{n_{\text{src}}^{\text{obs}}} \left\| \int_{X_{\text{rcv}} \subset \Gamma} (\mathbf{u}(\mathbf{f}_j, \mathbf{x}, \mathbf{m}) \cdot \mathbf{g}_k(\mathbf{x}) - \mathbf{d}_u(\mathbf{g}_k, \mathbf{x}) \cdot \mathbf{f}_j(\mathbf{x})) d\mathbf{x} \right\|^2. \quad (11)$$

To obtain the gradient, the backward problem correspond to a boundary value problem where the adjoint-sources, following the steps prescribed by Shi et al. (2019), are

$$\underline{\sigma} \cdot \mathbf{n} = \sum_{k=1}^{n_{\text{src}}^{\text{obs}}} \mathbf{g}_k(\mathbf{x}) \overline{\int_{X_{\text{rcv}} \subset \Gamma} (\mathbf{u}(\mathbf{f}_j, \mathbf{x}, \mathbf{m}) \cdot \mathbf{g}_k(\mathbf{x}) - \mathbf{d}_u(\mathbf{g}_k, \mathbf{x}) \cdot \mathbf{f}_j(\mathbf{x})) d\mathbf{x}}, \quad (12)$$

Nonetheless, as the source traction is imposed only at the position of the vibroseis base-plate (equal to zero elsewhere), it is unclear if it performs well. In the following experiment, we consider, per convenience, buried devices for the exploration acquisition setting.

## 2.6 Numerical implementation

To simulate the displacement and the stress tensor (or the strain), we implement the hybridizable discontinuous Galerkin (HDG) method (Arnold et al., 2002; Cockburn et al., 2009) for the discretization of equation 1. The motivation is that HDG solves the first-order problem (i.e., the system made of equations 1 and 2), hence gives access to both the displacement and stress tensor, while generating a linear system relatively small compared to other discretization approaches (Bonnasse-Gahot et al., 2017; Faucher and Scherzer, 2020).

The HDG method works in two steps. In the first step, the *global* linear system, whose matrix only accounts for the degrees of freedoms (dof) of the numerical trace for one variable (the displacement). In the second step, local (for each cell of the mesh), small systems are solved to have, from the numerical trace obtained at the global stage, the volume solutions for the displacement *and* for the stress tensor (Bonnasse-Gahot et al., 2017). In other discretization methods such as finite elements or internal penalty discontinuous Galerkin, upon discretization of the first-order problem equations 1 and 2, the resulting linear system is of size the number of dof for *all* unknowns (the stress tensor and the displacement). On the other hand, with the HDG method, the global linear system is smaller as it only takes the dof of the trace of one of the unknowns (the displacement). It makes it an appropriate choice for frequency-domain applications, where the bottleneck usually is the computational memory required to factorize the matrix and solve the linear system. We further refer to Kirby et al. (2012); Bonnasse-Gahot et al. (2017) and Faucher and Scherzer (2020) for more details on the HDG discretization and its performance. As it gives access to both solutions (stress and displacement) that are required for the reciprocity-gap misfit functional, the HDG method is also used in the acoustic settings of FRgWI by Faucher et al. (2020a).

## 3 Computational Experiment

We illustrate the performance of FRgWI with a two-dimensional isotropic elastic experiment where we consecutively use exploration and regional earthquake data. The data are generated using a domain of size  $28 \times 5 \text{ km}^2$  and we consider a domain of size  $22 \times 4.5 \text{ km}^2$  for the reconstruction, as illustrated in Figure 1. The elastic properties are pictured in Figures 2a, 2c and 2e, with the density, P-wave speed and S-wave speed respectively, and where we indicate



by white dashes the restriction to the inversion domain (from 4.5 to 22 km in  $x$  and from 0 to 4.5 km in depth). The model is composed of a body of high contrast in its center, with layered structures on the sides and below. In addition, there is a strong contrast in speeds between the layers.

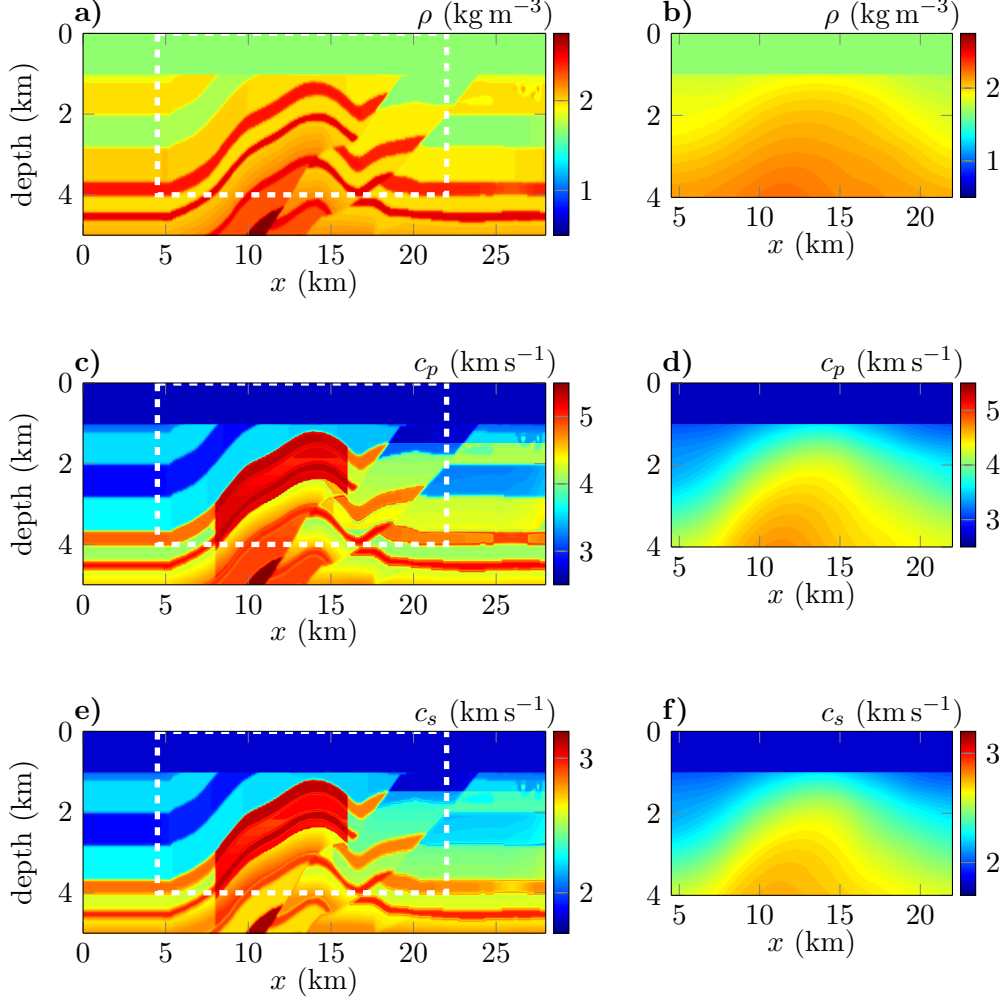


Figure 2: Target (a) density (c) P-wave speed and (e) S-wave speed models of size  $28 \times 5 \text{ km}^2$ , from which the observed measurements are generated. The white dashes indicate the imaging domain of size  $22 \times 4.5 \text{ km}^2$ , corresponding to the size of the initial (b) density (d) P-wave speed and (f) S-wave speed.

### 3.1 Multi-resolution reconstruction

For the reconstruction of the elastic physical properties, we follow the workflow described above, minimizing the misfit function  $\mathcal{J}$  of equation 6 and using both exploration and regional earthquake data.

1. In the first stage, we use data from regional events. There are ten passive sources ( $n_{\text{src}}^{\text{obs}} = 10$ ), whose positions are outside of the computational domain (Figure 1a). This is a relatively small data set but it contains usable low-frequencies, and we use contents from 0.2 Hz to 2 Hz.

2. In the second stage, we use data from an exploration acquisition setup, with  $n_{\text{src}}^{\text{obs}} = 89$  sources located at the surface. This data set is dense but does not contain low-frequencies below 2 Hz.

Despite using synthetic data, we incorporate white Gaussian noise in the measurements and use different meshes and order of polynomials between the generation of synthetic data and the inversion scheme. We assume the measurements are made by 359 receivers, located below the surface, every 50 m. The initial models for the reconstruction are shown in Figures 2b, 2d and 2f. In our experiment, we further assume the knowledge of the near-surface area where the parameters are taken constant (see Figure 1). This allows us to reduce the effect of the free-surface condition that generates reflections, increasing the non-linearity of the inversion procedure (Brossier et al., 2009). As an alternative, the use of a regularization term or a smoothing filter applied onto the gradient can also be used to balance the contributions of the free-surface (Guittou et al., 2012; Trinh et al., 2017).

With FRgWI, the choice of the sources for the computational acquisition is arbitrary (compared to more traditional misfit criterion which must respect the observational sources) and we take  $n_{\text{src}}^{\text{sim}} = 89$  computational sources, similarly to the exploration setup, for simplicity only. We refer to Faucher et al. (2020a) for more details on the flexibility in the choice and influence of these numerical sources, where the efficiency with respect to shot summation is investigated. In Figures 3a and 3b, we compare the gradient of the misfit functional with respect to the parameter  $1/\mu$  for the regional earthquake and the exploration data set, using the starting models of Figure 2, where we force to zero the upper (known) area. In both cases, the acquisition for the simulation (which is arbitrary with FRgWI) is using sources near the surface only, as mentioned above. For the regional earthquake data, we use a frequency of 0.2 Hz: we see in Figure 3a that the gradient shows long wavelength variations. We note higher amplitudes on the sides and bottom regions, that is, near where the passive sources are located, even if the computational ones are positioned near the surface. With the exploration data set (Figure 3b) we use a frequency of 2 Hz: we observe that the structures are smaller (higher wavenumber), with higher amplitudes in the upper part of the domain, where the exploration sources are located.

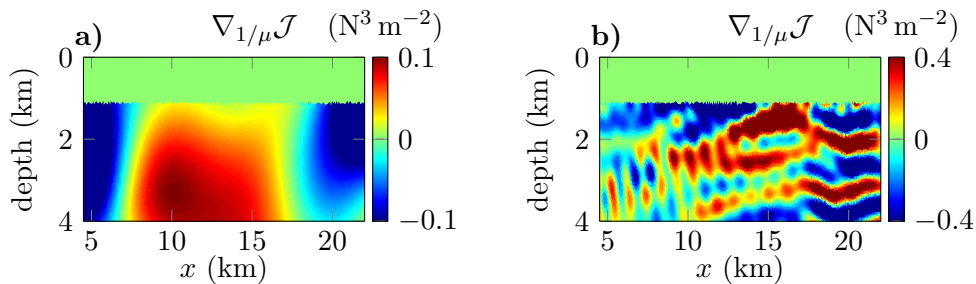


Figure 3: Comparison of the FRgWI gradient for the parameter  $1/\mu$  (a) using the regional earthquake data ( $n_{\text{src}}^{\text{obs}} = 10$  sources) at 0.2 Hz and (b) using the exploration data ( $n_{\text{src}}^{\text{obs}} = 89$  sources) at 2 Hz; both use the same acquisition for the simulations ( $n_{\text{src}}^{\text{sim}} = 89$  sources) and we force the values of the gradient to be zero in the layer where the parameters are known, according to Figure 1.

We follow a frequency continuation approach (Bunks et al., 1995; Faucher et al., 2020b), and perform 30 iterations per frequency. The first stage (using the data from passive sources) uses frequencies 0.2 Hz, 0.4 Hz, 0.6 Hz, 0.8 Hz, 1 Hz and 2 Hz. The second stage with the exploration data set uses frequencies from 2 Hz to 10 Hz, every 1 Hz. While the density is not

updated, this lack of information should not prevent us from recovering the other parameters and we further select the parametrization  $1/\lambda$  and  $1/\mu$  for the inversion (Faucher, 2017). The results after the iterations with the low-frequency regional earthquake data are pictured in Figures 4c and 4d, where we visualize the wave speeds (equation 4). Then, these reconstructed models serve as initial ones to carry on the reconstruction with the exploration data. The results are shown in Figures 4a and 4b.

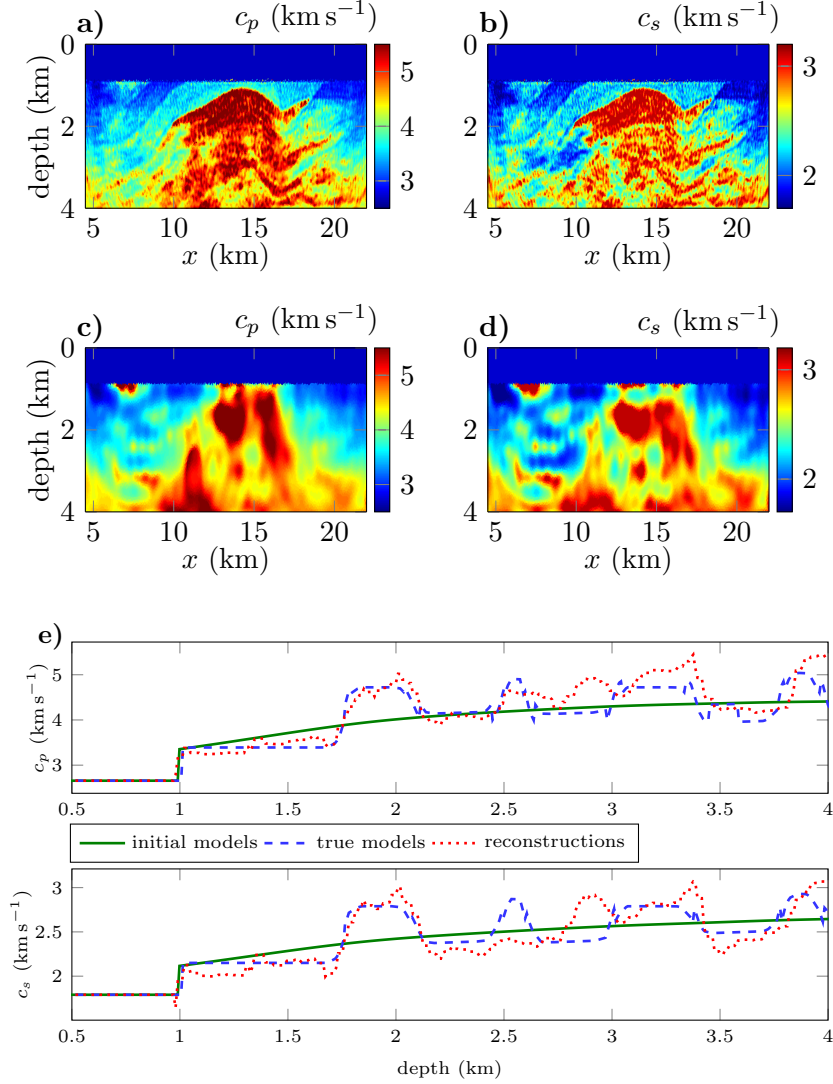


Figure 4: The reconstructed (a) P-wave speed and (b) S-wave speed models use the exploration data from 2 Hz to 10 Hz, starting from the (c) P-wave speed and (d) S-wave speed models built with the low-frequency data from regional events. (e) Vertical sections of the target, starting and reconstructed models at  $x = 16.5$  km.

The low-frequency reconstruction provides the background profile of the parameters, and is able to discover the contrasting body in the center. As expected, the parameters are smooth at this stage, with only the long wavelengths investigated. Despite the use of data from few passive sources located outside the inverted area, the inversion procedure gives access to the low-frequency profiles of the medium parameters. In the second stage, the reconstruction of the higher wavenumbers is obtained from the exploration data. Eventually, we see in

Figure 4 that the upper part of the contrast is correctly recovered. Some of the underneath layers appear, but the deep and side parts of the models are mostly missing due to the limited illumination, as highlighted in the vertical section in  $x = 16.5$  km in Figure 4e.

### 3.2 Comparison of misfit functions in the second stage

In the first stage with the data from the regional events, the FRgWI method is essential as it does not require the positions of the passive sources. However, in the second stage with the exploration data, it is common to assume the knowledge of the sources (e.g., the position of the vibroseis truck) and thus it is possible to rely on a more traditional misfit criterion, by evaluating the difference between the observed and simulated data as follows:

$$\mathcal{J}_0(\mathbf{m}) = \sum_{k=1}^{n_{\text{src}}^{\text{obs}}} \frac{1}{2} \left\| \mathcal{F}_u(\mathbf{g}_k, \mathbf{m}) - \mathbf{d}_u(\mathbf{g}_k) \right\|^2 + \frac{1}{2} \left\| \mathcal{F}_\epsilon(\mathbf{g}_k, \mathbf{m}) - \mathbf{d}_\epsilon(\mathbf{g}_k) \right\|^2, \quad (13)$$

where the forward problem is defined in equation 5. Here, contrary to our misfit function equation 8, the observational sources  $\mathbf{g}$  must be used to generate the simulations.

Now, starting from the models recovered after the first stage using the low frequencies in Figures 4c and 4d, we perform the minimization of  $\mathcal{J}_0$  (equation 13) using the exploration data set. We compare the evolution of the cost functions for the first frequency of the exploration data set, 2 Hz, in Figure 5a. While  $\mathcal{J}$  allows the flexibility of the computational sources ( $\mathbf{f}$  in equation 8), we use the same set as the observational ones (i.e.,  $\mathbf{g}$ ) to have a consistent comparison between the two methods. In Figure 5b, we provide the evolution of the relative model error, defined as,

$$\epsilon_k(c, \mathcal{J}) = \left\| \frac{c_k(\mathcal{J}) - c^\dagger}{c^\dagger} \right\|, \quad (14)$$

where  $c_k(\mathcal{J})$  represents the current reconstructed wave speed at iteration  $k$  using the misfit functional  $\mathcal{J}$ , and  $c^\dagger$  stands for the true wave speeds, displayed in Figures 2c and 2e. Here, to compute the  $L^2$ -norm  $\| \cdot \|$ , the two-dimensional models are represented on a Cartesian grid with  $2251 \times 901 = 2\,028\,151$  coefficients.

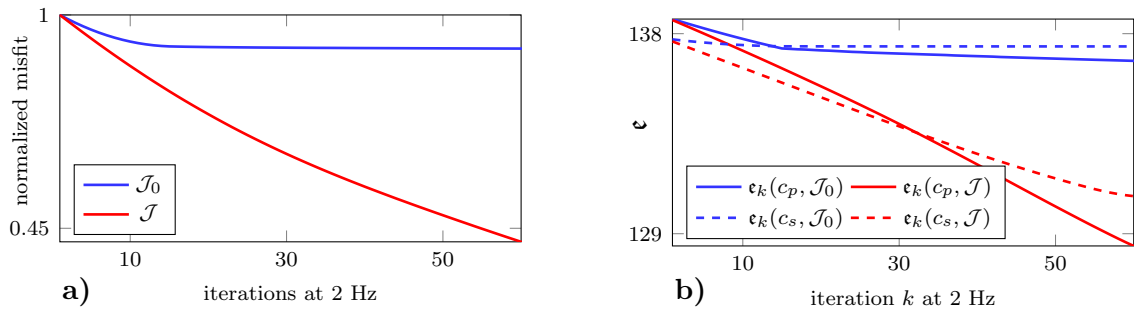


Figure 5: Comparison of performance in the minimization of the misfit functionals  $\mathcal{J}$  and  $\mathcal{J}_0$  in equations 8 and 13, respectively. The minimizations use the exploration data at 2 Hz, starting from the initial models built with the FRgWI method and the low-frequency regional earthquake data shown in Figures 4c and 4d. In order to use  $\mathcal{J}_0$ , the computational sources must coincide with the observational ones; the iterative minimization relies on the non-linear conjugate gradient method (Nocedal and Wright, 2006). (a) Evolution of the normalized misfit functionals (i.e., scaled with its value at the first iteration) and (b) relative error for the P- and S-wave speeds (equation 14), for the iterations at 2 Hz frequency.

FRgWI improves drastically the convergence rate of the iterative minimization compared to the standard misfit function  $\mathcal{J}_0$ . We see that  $\mathcal{J}_0$  stagnates rapidly in Figure 5a, after about 15 iterations while in the FRgWI method,  $\mathcal{J}$  keeps decreasing even after 60 iterations. The improvement given by the FRgWI method is confirmed in terms of model error in Figure 5b, which keeps decreasing for both the P- and S-wave speed models. We further note how the P-wave speed model keeps improving compared to the S one. On the contrary, the relative model error associated to  $\mathcal{J}_0$  stagnates after a few iterations, similar to the cost function in Figure 5a.

In Figure 6, we show the reconstructed P- and S-wave speeds obtained by minimizing  $\mathcal{J}_0$  in equation 13, using the exploration data set with frequencies from 2 Hz to 10 Hz. The inversion procedure starts from the initial models built with the FRgWI method and the regional earthquake data displayed in Figures 4c and 4d. Indeed, the stage one (inversion using the low-frequency regional earthquake data) can only be performed with the FRgWI method, which does not necessitate the knowledge (positions and functions) of the passive sources, hence we compare the minimization for the stage two only.

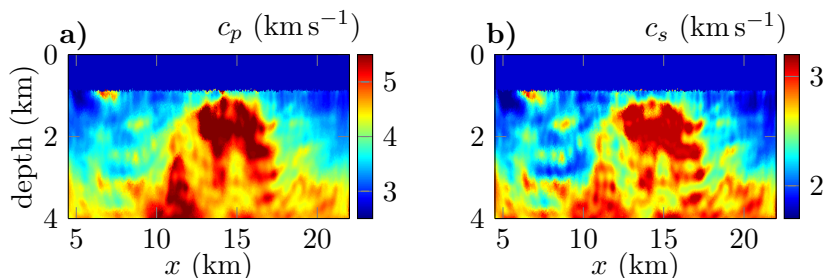


Figure 6: The reconstructed (a) P-wave speed and (b) S-wave speed models obtained from the minimization of  $\mathcal{J}_0$  in equation 13. The inversion uses the exploration data from 2 Hz to 10 Hz, starting from the models built with the FRgWI method and the low-frequency regional earthquake data in Figures 4c and 4d. The reconstructions obtained with the FRgWI method and minimization of  $\mathcal{J}$  in equation 8 are displayed in Figures 4a and 4b for comparison.

The rapid stagnation of the misfit function and model errors in Figure 5 is confirmed by the pictures of the properties reconstructed (Figures 6a and 6b) from the minimization of  $\mathcal{J}_0$  in equation 13 using frequencies from 2 Hz to 10 Hz. We see that the iterative minimization algorithm barely modifies the initial models given in Figures 4c and 4d. These reconstructed models are particularly inaccurate compared to the reconstructions obtained from the minimization of  $\mathcal{J}$  in equation 8 which are pictured in Figures 4a and 4b.

In the same configuration, that is, when the computational sources are selected to coincide with the observational ones and when we start from the same initial guess, we see that the FRgWI method behaves better than the least-squares criterion. In addition, the FRgWI allows for arbitrary computational sources, thus offering more flexibility: for instance the stage one of the inversion using the regional earthquake data cannot be performed with the least-squares criterion of equation 13.

## 4 Discussion

The main feature of FRgWI is that the sources that generate the measurements do *not* have to correspond with the sources that are used for the simulations and the misfit function then tests each of the measured data with every simulation. In this work, we have experimented

the use of data from events (observational sources) located outside the computational domain without requiring any pre-processing. With FRgWI, we do *not* need to know the precise origin of the (passive) source and we do *not* have to produce simulations on the large domain where the event has occurred. Contrary to conventional teleseismic inversion which needs distant earthquake to work with plane wave illumination, FRgWI allows for any type of passive sources, hence enabling the use of data from local events. The use of data from regional (or teleseismic) events compensates for the lack of low-frequency contents in the exploration data, and are used as a first step to build initial models. As the method requires numerical simulations of the displacement and stress, the HDG discretization is an appropriate candidate to solve numerically the forward problem, by working with the first-order system at a reduced computational cost. We have implemented the method in the frequency domain, which can make it difficult to handle large media in three-dimensions, due to the memory requirement. Nonetheless, the method can similarly work in the time (or hybrid) domain, using a frequency continuation approach (Bunks et al., 1995). The resulting cross-correlations in the misfit function should not lead to any additional computational difficulties and the time domain allows to account for larger domains.

We have provided a pilot study to illustrate the possibilities offered by the FRgWI method: it now needs to be applied on more practical settings. While the formulation of the misfit functional in terms of the stress remains identical with anisotropy (equation 6), it implies that measurements of the complete strain tensor have to be obtained. The misfit functional is defined from the integral over the receiver surface such that, in the case of topography, the method can be applied provided the surface is Lipschitz. The misfit can be evaluated via a quadrature rule, that is, weighting the contribution of the receivers depending on their positions. This is the subject of ongoing research.

Another possible extension of the FRgWI method is by including attenuation, which is relatively straightforward in the frequency-domain: its incorporation maintains the constitutive law in equation 2 with a complex-valued elasticity tensor (Bland, 1960; Carcione, 2007). However, in the time-domain, the constitutive law for a medium with attenuation incorporates time derivatives of the strain and/or stress (Carcione, 2007), and the reciprocity formula would have to be derived accordingly. While the misfit functional allows to work with observational sources at arbitrary positions, as we have illustrated, it also allows for the arbitrary positions and functions of the computational ones. Consequently, FRgWI a good candidate for shot-stacking (source summation), as highlighted by Faucher et al. (2020a) in the acoustic case. In addition, while we have used computational sources near the surface only, using alternative positions should be investigated, as well as other source types and geometries (e.g., using plane-waves). Namely, the experiment we have carried out is the first step to analyze the potential of the method.

## 5 Conclusion

We implement a new misfit functional for elastic reconstruction of Earth parameters, and have shown a preliminary experiment which illustrates its flexibility regarding the acquisition setups. The underlying FRgWI method opens up the perspective of considering passive-source data for exploration, in order to recover the low-wavenumbers subsurface models. These low-frequencies, missing in the exploration data, are crucial to build smooth background models and to mitigate cycle-skipping issues during inversion.

Applications of the FRgWI method directly relates to the ability of the new acquisition techniques with fiber optic cable in DAS to obtain the strain. Nonetheless, it is still difficult to rely on the availability of such data for practical applications. For instance, the precise



orientation of the fiber can be hard to control. Our study remains conceptual at this stage and the accuracy of the required DAS technology and the available bandwidth of such measurements must be addressed. Then, the implementation of the method from the strain also requires the values of the medium parameters (except the density) along the cable. Future applications should follow the steps: (1) reconstruction of the very near-surface elastic parameters using the (surface) exploration data, (2) minimization of the sub-surface reciprocity functional using the regional earthquake data to recover the low wavenumbers of the models and (3) reconstruction of the high wavenumbers with the exploration data. In this work, we carried out a pilot computational experiment to study the capability of our approach and to illustrate how to exploit DAS.

## Acknowledgments

The authors also thank Jonathan Ajo-Franklin for interesting discussions on Distributed Acoustic Sensing. The research of FF is supported by the Austrian Science Fund (FWF) under the Lise Meitner fellowship M 2791-N. MVdH was supported by the Simons Foundation under the MATH+X program, the National Science Foundation under grant DMS-1815143, and the corporate members of the Geo-Mathematical Imaging Group at Rice University, USA. OS is supported by the FWF, with SFB F68, project F6807-N36 (Tomography with Uncertainties).

The code used for the experiments, `hawen`, is developed by the first author and available at <https://ffaucher.gitlab.io/hawen-website/>. The scripts and data-set to reproduce the results are archived at <http://phaidra.univie.ac.at/o:1097637>.

## References

- Ajo-Franklin, J., Lindsey, N., Daley, T., Freifeld, B., Robertson, M., Ulrich, C., Dou, S., Martin, E., and Wagner, A. (2015). A field test of distributed acoustic sensing for ambient noise recording. pages 2620–2624. 85th Annual International Meeting, SEG, Expanded Abstracts.
- Ajo-Franklin, J. B., Dou, S., Lindsey, N. J., Monga, I., Tracy, C., Robertson, M., Tribaldos, V. R., Ulrich, C., Freifeld, B., Daley, T., et al. (2019). Distributed acoustic sensing using dark fiber for near-surface characterization and broadband seismic event detection. *Scientific reports*, 9(1):1–14.
- Aki, K. and Richards, P. G. (2002). *Quantitative seismology: Theory and Methods*. University Science Books.
- Alessandrini, G., De Hoop, M. V., Faucher, F., Gaburro, R., and Sincich, E. (2019). Inverse problem for the Helmholtz equation with Cauchy data: reconstruction with conditional well-posedness driven iterative regularization. *ESAIM: M2AN*, 53:1005–1030.
- Arnold, D. N., Brezzi, F., Cockburn, B., and Marini, L. D. (2002). Unified analysis of discontinuous Galerkin methods for elliptic problems. *SIAM journal on numerical analysis*, 39(5):1749–1779.
- Baeten, G. J. M. (1989). *Theoretical and practical aspects of the Vibroseis method*. PhD thesis, Technische Universiteit Delft.

- Bamberger, A., Chavent, G., and Lailly, P. (1977). Une application de la théorie du contrôle à un problème inverse de sismique. *Annales de Géophysique*, 33:183–200.
- Bamberger, A., Chavent, G., and Lailly, P. (1979). About the stability of the inverse problem in the 1-d wave equation. *Journal of Applied Mathematics and Optimisation*, 5:1–47.
- Barucq, H., Chavent, G., and Faucher, F. (2019). A priori estimates of attraction basins for nonlinear least squares, with application to Helmholtz seismic inverse problem. *Inverse Problems*, 35:115004.
- Beller, S., Monteiller, V., Combe, L., Operto, S., and Nolet, G. (2018a). On the sensitivity of teleseismic full-waveform inversion to earth parametrization, initial model and acquisition design. *Geophysical Journal International*, 212:1344–1368.
- Beller, S., Monteiller, V., Operto, S., Nolet, G., Paul, A., and Zhao, L. (2018b). Lithospheric architecture of the South-Western Alps revealed by multiparameter teleseismic full-waveform inversion. *Geophysical Journal International*, 212:1369–1388.
- Beretta, E., de Hoop, M. V., Faucher, F., and Scherzer, O. (2016). Inverse boundary value problem for the Helmholtz equation: quantitative conditional Lipschitz stability estimates. *SIAM Journal on Mathematical Analysis*, 48(6):3962–3983.
- Beretta, E., de Hoop, M. V., Francini, E., Vessella, S., and Zhai, J. (2017). Uniqueness and Lipschitz stability of an inverse boundary value problem for time-harmonic elastic waves. *Inverse Problems*, 33(3):035013.
- Beretta, E., Francini, E., and Vessella, S. (2014). Uniqueness and Lipschitz stability for the identification of lamé parameters from boundary measurements. *Inverse Problems & Imaging*, 8(1930-8337\_2014\_3\_611):611–644.
- Bland, D. R. (1960). *The theory of linear viscoelasticity*. Courier Dover Publications.
- Bonnasse-Gahot, M., Calandra, H., Diaz, J., and Lanteri, S. (2017). Hybridizable discontinuous Galerkin method for the 2D frequency-domain elastic wave equations. *Geophysical Journal International*, 213(1):637–659.
- Bostock, M., Rondenay, S., and Shragge, J. (2001). Multiparameter two-dimensional inversion of scattered teleseismic body waves 1. Theory for oblique incidence. *Journal of Geophysical Research: Solid Earth*, 106:30771–30782.
- Bozdağ, E., Peter, D., Lefebvre, M., Komatitsch, D., Tromp, J., Hill, J., Podhorszki, N., and Pugmire, D. (2016). Global adjoint tomography: first-generation model. *Geophysical Journal International*, 207(3):1739–1766.
- Brossier, R., Operto, S., and Virieux, J. (2009). Seismic imaging of complex onshore structures by 2D elastic frequency-domain full-waveform inversion. *Geophysics*, 74:WCC105–WCC118.
- Brossier, R., Operto, S., and Virieux, J. (2010). Which data residual norm for robust elastic frequency-domain full waveform inversion? *Geophysics*, 75:R37–R46.
- Bunks, C., Saleck, F. M., Zaleski, S., and Chavent, G. (1995). Multiscale seismic waveform inversion. *Geophysics*, 60:1457–1473.

- Caday, P., de Hoop, M., Katsnelson, V., and Uhlmann, G. (2019). Reconstruction of piecewise smooth wave speeds using multiple scattering. *Transactions of the American Mathematical Society*, 372(2):1213–1235.
- Carcione, J. M. (2007). *Wave fields in real media: Wave propagation in anisotropic, anelastic, porous and electromagnetic media*. Elsevier.
- Chavent, G. (1974). Identification of functional parameters in partial differential equations. In Goodson, R. E. and Polis, M., editors, *Identification of Parameters in Distributed Systems*, pages 31–48. American Society of Mechanical Engineer, New York.
- Chavent, G. (2010). *Nonlinear least squares for inverse problems: theoretical foundations and step-by-step guide for applications*. Springer Science & Business Media.
- Choi, Y. and Alkhalifah, T. (2011). Source-independent time-domain waveform inversion using convolved wavefields: Application to the encoded multisource waveform inversion. *Geophysics*, 76(5):R125–R134.
- Clément, F., Chavent, G., and Gómez, S. (2001). Migration-based travelttime waveform inversion of 2-d simple structures: A synthetic example. *Geophysics*, 66:845–860.
- Cockburn, B., Gopalakrishnan, J., and Lazarov, R. (2009). Unified hybridization of discontinuous Galerkin, mixed, and continuous Galerkin methods for second order elliptic problems. *SIAM Journal on Numerical Analysis*, 47(2):1319–1365.
- Colton, D. and Haddar, H. (2005). An application of the reciprocity gap functional to inverse scattering theory. *Inverse Problems*, 21(1):383–398.
- Cox, B., Wills, P., Kiyashchenko, D., Mestayer, J., Lopez, J., Bourne, S., Lupton, R., Solano, G., Henderson, N., Hill, D., et al. (2012). Distributed acoustic sensing for geophysical measurement, monitoring and verification. *CSEG Recorder*, 37(2):7–13.
- Daley, T. M., Freifeld, B. M., Ajo-Franklin, J., Dou, S., Pevzner, R., Shulakova, V., Kashikar, S., Miller, D. E., Goetz, J., and Henningses, J. (2013). Field testing of fiber-optic distributed acoustic sensing (DAS) for subsurface seismic monitoring. *The Leading Edge*, 32(6):699–706.
- de Hoop, M. V. and de Hoop, A. T. (2000). Wave-field reciprocity and optimization in remote sensing. *Proceedings of the Royal Society of London. Series A: Mathematical, Physical and Engineering Sciences*, 456(1995):641–682.
- de Hoop, M. V., Qiu, L., and Scherzer, O. (2015). An analysis of a multi-level projected steepest descent iteration for nonlinear inverse problems in Banach spaces subject to stability constraints. *Numerische Mathematik*, 129(1):127–148.
- Drijkoningen, G. G., Rademakers, F., Slob, E. C., and Fokkema, J. T. (2006). A new elastic model for ground coupling of geophones with spikes. *Geophysics*, 71:Q9–Q17.
- Faucher, F. (2017). *Contributions to seismic full waveform inversion for time harmonic wave equations: stability estimates, convergence analysis, numerical experiments involving large scale optimization algorithms*. PhD thesis, Université de Pau et Pays de l’Ardour.
- Faucher, F., Alessandrini, G., Barucq, H., de Hoop, M., Gaburro, R., and Sincich, E. (2020a). Full reciprocity-gap waveform inversion, enabling sparse-source acquisition. *Geophysics*, 85:A37–V441.

- Faucher, F., Chavent, G., Barucq, H., and Calandra, H. (2020b). A priori estimates of attraction basins for velocity model reconstruction by time-harmonic full-waveform inversion and data-space reflectivity formulation. *Geophysics*, 85:R223–R241.
- Faucher, F. and Scherzer, O. (2020). Adjoint-state method for Hybridizable Discontinuous Galerkin discretization, application to the inverse acoustic wave problem. *Computer Methods in Applied Mechanics and Engineering*, 372:113406.
- Fichtner, A. (2010). *Full seismic waveform modelling and inversion*. Springer Science & Business Media.
- Fichtner, A., Bunge, H.-P., and Igel, H. (2006a). The adjoint method in seismology: I. Theory. *Physics of the Earth and Planetary Interiors*, 157(1-2):86–104.
- Fichtner, A., Bunge, H.-P., and Igel, H. (2006b). The adjoint method in seismology: II. Applications: traveltimes and sensitivity functionals. *Physics of the Earth and Planetary Interiors*, 157(1-2):105–123.
- Fichtner, A., Kennett, B. L., Igel, H., and Bunge, H.-P. (2008). Theoretical background for continental-and global-scale full-waveform inversion in the time–frequency domain. *Geophysical Journal International*, 175(2):665–685.
- Fichtner, A. and Trampert, J. (2011). Hessian kernels of seismic data functionals based upon adjoint techniques. *Geophysical Journal International*, 185(2):775–798.
- Gauthier, O., Virieux, J., and Tarantola, A. (1986). Two-dimensional nonlinear inversion of seismic waveforms; numerical results. *Geophysics*, 51(7):1387–1403.
- Givoli, D. and Keller, J. B. (1990). Non-reflecting boundary conditions for elastic waves. *Wave motion*, 12(3):261–279.
- Glowinski, R. (1985). *Numerical Methods for Nonlinear Variational Problems*. Springer-Verlag.
- Guitton, A., Ayeni, G., and Díaz, E. (2012). Constrained full-waveform inversion by model reparameterization. *Geophysics*, 77(2):R117–R127.
- Higdon, R. L. (1991). Absorbing boundary conditions for elastic waves. *Geophysics*, 56(2):231–241.
- Innanen, K. (2017). Determination of seismic-tensor strain from helical wound cable-distributed acoustic sensing cable with arbitrary and nested-helix winds. pages 926–930. 87th Annual International Meeting, SEG, Expanded Abstracts.
- Jousset, P., Reinsch, T., Ryberg, T., Blanck, H., Clarke, A., Aghayev, R., Hersir, G. P., Henniges, J., Weber, M., and Krawczyk, C. M. (2018). Dynamic strain determination using fibre-optic cables allows imaging of seismological and structural features. *Nature communications*, 9(1):1–11.
- Kirby, R. M., Sherwin, S. J., and Cockburn, B. (2012). To cg or to hdg: a comparative study. *Journal of Scientific Computing*, 51(1):183–212.
- Kohn, R. V. and Vogelius, M. (1985). Determining conductivity by boundary measurements ii. interior results. *Communications on Pure and Applied Mathematics*, 38(5):643–667.

- Komatitsch, D., Xie, Z., Bozdağ, E., Sales de Andrade, E., Peter, D., Liu, Q., and Tromp, J. (2016). Anelastic sensitivity kernels with parsimonious storage for adjoint tomography and full waveform inversion. *Geophysical Journal International*, 206(3):1467–1478.
- Lailly, P. (1983). The seismic inverse problem as a sequence of before stack migrations. In Bednar, J. B., editor, *Conference on Inverse Scattering: Theory and Application*, pages 206–220. Society for Industrial and Applied Mathematics.
- Lellouch, A., Yuan, S., Spica, Z., Biondi, B., and Ellsworth, W. (2019). Seismic velocity estimation using passive downhole distributed acoustic sensing records: Examples from the San Andreas fault observatory at depth. *Journal of Geophysical Research: Solid Earth*, 124:6931–6948.
- Lim Chen Ning, I. and Sava, P. (2018). Multicomponent distributed acoustic sensing: Concept and theory. *Geophysics*, 83:P1–P8.
- Lindsey, N. J., Martin, E. R., Dreger, D. S., Freifeld, B., Cole, S., James, S. R., Biondi, B. L., and Ajo-Franklin, J. B. (2017). Fiber-optic network observations of earthquake wavefields. *Geophysical Research Letters*, 44:11–792.
- Lindsey, N. J., Rademacher, H., and Ajo-Franklin, J. B. (2020). On the broadband instrument response of fiber-optic DAS arrays. *Journal of Geophysical Research: Solid Earth*, 125(2):e2019JB018145.
- Lions, J. L. (1971). *Optimal control of systems governed by partial differential equations*. Springer.
- Liu, Q. and Tromp, J. (2008). Finite-frequency sensitivity kernels for global seismic wave propagation based upon adjoint methods. *Geophysical Journal International*, 174(1):265–286.
- Luo, Y. and Schuster, G. T. (1991). Wave-equation traveltime inversion. *Geophysics*, 56(5):645–653.
- Luo, Y., Zhu, H., Nissen-Meyer, T., Morency, C., and Tromp, J. (2009). Seismic modeling and imaging based upon spectral-element and adjoint methods. *The Leading Edge*, 28(5):568–574.
- Masson, Y. and Romanowicz, B. (2017). Box tomography: localized imaging of remote targets buried in an unknown medium, a step forward for understanding key structures in the deep earth. *Geophysical Journal International*, 211(1):141–163.
- Mateeva, A., Lopez, J., Mestayer, J., Wills, P., Cox, B., Kiyashchenko, D., Yang, Z., Berlang, W., Detomo, R., and Grandi, S. (2013). Distributed acoustic sensing for reservoir monitoring with VSP. *The Leading Edge*, 32(10):1278–1283.
- Mestayer, J., Cox, B., Wills, P., Kiyashchenko, D., Lopez, J., Costello, M., Bourne, S., Ugueto, G., Lupton, R., Solano, G., et al. (2011). Field trials of distributed acoustic sensing for geophysical monitoring. pages 4253–4257. 81th Annual International Meeting, SEG, Expanded Abstracts.
- Métivier, L., Brossier, R., Mérigot, Q., Oudet, E., and Virieux, J. (2016). Measuring the misfit between seismograms using an optimal transport distance: application to full waveform inversion. *Geophysical Journal International*, 205(1):345–377.

- Métivier, L., Brossier, R., Virieux, J., and Operto, S. (2013). Full waveform inversion and the truncated Newton method. *SIAM Journal on Scientific Computing*, 35(2):B401–B437.
- Modrak, R. and Tromp, J. (2016). Seismic waveform inversion best practices: regional, global and exploration test cases. *Geophysical Journal International*, 206(3):1864–1889.
- Montagner, J.-P., Larmat, C., Capdeville, Y., Fink, M., Phung, H., Romanowicz, B., Clévéde, E., and Kawakatsu, H. (2012). Time-reversal method and cross-correlation techniques by normal mode theory: a three-point problem. *Geophysical Journal International*, 191(2):637–652.
- Mora, P. (1987). Nonlinear two-dimensional elastic inversion of multioffset seismic data. *Geophysics*, 52(9):1211–1228.
- Nocedal, J. and Wright, S. J. (2006). *Numerical Optimization*. Springer Series in Operations Research, 2 edition.
- Plessix, R.-E. (2006). A review of the adjoint-state method for computing the gradient of a functional with geophysical applications. *Geophysical Journal International*, 167:495–503.
- Pratt, R. G. (1999). Seismic waveform inversion in the frequency domain, part 1: Theory and verification in a physical scale model. *Geophysics*, 64(3):888–901.
- Pratt, R. G., Shin, C., and Hick, G. J. (1998). Gauss–newton and full newton methods in frequency–space seismic waveform inversion. *Geophysical Journal International*, 133(2):341–362.
- Pratt, R. G., Song, Z.-M., Williamson, P., and Warner, M. (1996). Two-dimensional velocity models from wide-angle seismic data by wavefield inversion. *Geophysical Journal International*, 124(2):323–340.
- Ravaut, C., Operto, S., Improta, L., Virieux, J., Herrero, A., and Dell’Aversana, P. (2004). Multiscale imaging of complex structures from multifold wide-aperture seismic data by frequency-domain full-waveform tomography: Application to a thrust belt. *Geophysical Journal International*, 159(3):1032–1056.
- Robertsson, J. O. and Chapman, C. H. (2000). An efficient method for calculating finite-difference seismograms after model alterations. *Geophysics*, 65(3):907–918.
- Rondenay, S., Bostock, M., and Shragge, J. (2001). Multiparameter two-dimensional inversion of scattered teleseismic body waves 3. Application to the Cascadia 1993 data set. *Journal of Geophysical Research: Solid Earth*, 106:30795–30807.
- Shi, J., Beretta, E., de Hoop, M. V., Francini, E., and Vessella, S. (2019). A numerical study of multi-parameter full waveform inversion with iterative regularization using multi-frequency vibroseis data. *Computational Geosciences*, pages 1–19.
- Shragge, J., Bostock, M., and Rondenay, S. (2001). Multiparameter two-dimensional inversion of scattered teleseismic body waves 2. Numerical examples. *Journal of Geophysical Research: Solid Earth*, 106:30783–30793.
- Sirgue, L. and Pratt, R. G. (2004). Efficient waveform inversion and imaging: A strategy for selecting temporal frequencies. *Geophysics*, 69:231–248.



- Spikes, K. T., Tisato, N., Hess, T. E., and Holt, J. W. (2019). Comparison of geophone and surface-deployed distributed acoustic sensing seismic data. *Geophysics*, 84:A25–A29.
- Symes, W. and Carazzone, J. J. (1991). Velocity inversion by differential semblance optimization. *Geophysics*, 56:654–663.
- Tape, C., Liu, Q., and Tromp, J. (2007). Finite-frequency tomography using adjoint methods – Methodology and examples using membrane surface waves. *Geophysical Journal International*, 168(3):1105–1129.
- Tarantola, A. (1984). Inversion of seismic reflection data in the acoustic approximation. *Geophysics*, 49:1259–1266.
- Ten Kroode, F., Bergler, S., Corsten, C., de Maag, J. W., Strijbos, F., and Tijhof, H. (2013). Broadband seismic data – The importance of low frequencies. *Geophysics*, 78:WA3–WA14.
- Trinh, P.-T., Brossier, R., Métivier, L., Virieux, J., and Wellington, P. (2017). Bessel smoothing filter for spectral-element mesh. *Geophysical Journal International*, 209(3):1489–1512.
- Tromp, J. (2019). Seismic wavefield imaging of earth’s interior across scales. *Nature Reviews Earth & Environment*, pages 1–14.
- Tromp, J., Tape, C., and Liu, Q. (2005). Seismic tomography, adjoint methods, time reversal and banana-doughnut kernels. *Geophysical Journal International*, 160(1):195–216.
- Van Leeuwen, T. and Mulder, W. (2010). A correlation-based misfit criterion for wave-equation travelttime tomography. *Geophysical Journal International*, 182(3):1383–1394.
- Virieux, J. and Operto, S. (2009). An overview of full-waveform inversion in exploration geophysics. *Geophysics*, 74:WCC1–WCC26.
- Wang, H. F., Zeng, X., Miller, D. E., Fratta, D., Feigl, K. L., Thurber, C. H., and Mellors, R. J. (2018). Ground motion response to an ML 4.3 earthquake using co-located distributed acoustic sensing and seismometer arrays. *Geophysical Journal International*, 213:2020–2036.
- Wang, Z., Navon, I. M., Le Dimet, F.-X., and Zou, X. (1992). The second order adjoint analysis: theory and applications. *Meteorology and atmospheric physics*, 50(1-3):3–20.
- Yang, Y., Engquist, B., Sun, J., and Hamfeldt, B. F. (2018). Application of optimal transport and the quadratic wasserstein metric to full-waveform inversion. *Geophysics*, 83:R43–R62.